











Probing the reach of the Intermediate Polar Cataclysmic Variable Population with Swift J183920.1-045350

NICHOLAS M. GORGONE ^{1,2}, PATRICK A. WOUTD ³, DAVID BUCKLEY ⁴, KOJI MUKAI,^{5,6} CHRYSSA KOUVELIOTOU,⁷
ERSIN GÖĞÜŞ ⁷, ERIC BELLM ⁸, JUSTIN D. LINFORD ⁹, ALEXANDER J. VAN DER HORST,^{1,2} MATTHEW G. BARING ¹⁰,
DIETER HARTMANN ¹¹, PAUL BARRETT ¹, BRADLEY CENKO,^{12,13} MELISSA GRAHAM,⁸ JOHNATHAN GRANOT,^{1,14}
FIONA HARRISON,¹⁵ JAMIE KENNEA,¹⁶ BRENDAN M. O'CONNOR ^{1,2}, STEPHEN POTTER,⁴ DANIEL STERN,¹⁷ AND
RALPH WIJERS¹⁸

¹*Department of Physics, The George Washington University, Washington, DC 20052, USA*

²*Astronomy, Physics and Statistics Institute of Sciences (APSIS), The George Washington University, Washington, DC 20052, USA*

³*Department of Astronomy, University of Cape Town, Private Bag X3, Rondebosch 7701, South Africa*

⁴*South African Astronomical Observatory, P.O. Box 9, 7935 Observatory, South Africa*

⁵*CRESST II and X-ray Astrophysics Laboratory, NASA/GSFC, Greenbelt, MD 20771, USA*

⁶*Department of Physics, University of Maryland Baltimore County, 1000 Hilltop Circle, Baltimore MD 21250, USA*

⁷*Sabancı University, Faculty of Engineering and Natural Sciences, İstanbul 34956 Turkey*

⁸*DIRAC Institute, Department of Astronomy, University of Washington, 3910 15th Avenue NE, Seattle, WA 98195, USA*

⁹*National Radio Astronomy Observatory, P.O. Box O, Socorro, NM 87801, USA*

¹⁰*Department of Physics and Astronomy - MS 108, Rice University, 6100 Main Street, Houston, Texas 77251-1892, USA*

¹¹*Department of Physics and Astronomy, Clemson University, Kinard Lab of Physics, Clemson, SC 29634-0978, USA*

¹²*Astrophysics Science Division, NASA Goddard Space Flight Center, MC 661, Greenbelt, MD 20771, USA*

¹³*Joint Space-Science Institute, University of Maryland, College Park, MD 20742, USA*

¹⁴*Department of Natural Sciences, The Open University of Israel, P.O. Box 808, Ra'anana 43537, Israel*

¹⁵*Cahill Center for Astrophysics, California Institute of Technology, 1216 East California Boulevard, Pasadena, CA 91125, USA*

¹⁶*Department of Astronomy and Astrophysics, The Pennsylvania State University, 525 Davey Lab, University Park, PA 16802, USA*

¹⁷*Jet Propulsion Laboratory, California Institute of Technology, 4800 Oak Grove Drive, Mail Stop 169-221, Pasadena, CA 91109, USA*

¹⁸*University of Amsterdam, Science Park 904, 1098 XH Amsterdam, The Netherlands*

ABSTRACT

We report on the *Swift*/XRT Deep Galactic Plane Survey discovery and multi-wavelength follow-up observations of a new intermediate polar Cataclysmic Variable, Swift J183920.1–045350. A 449.7 s spin period is found in *XMM-Newton* and *NuSTAR* data, accompanied by a 459.9 s optical period that is most likely the synodic, or beat period, produced from a 5.6 h orbital period. The orbital period is seen with moderate significance in independent long-baseline optical photometry observations with ZTF and SAAO. We find that the source X-ray pulsed fraction decreases with increasing energy. The X-ray spectra are consistent with the presence of an Fe emission line complex with both local and interstellar absorption. In the optical spectra, strong H α , H I, He I and He II emission lines are observed, all common features in magnetic CVs. The source properties are thus typical of known intermediate polars, with the exception of its estimated distance of $2.26_{-0.83}^{+1.93}$ kpc, which is larger than typical, extending the reach of the CV population in our Galaxy.

Keywords: Cataclysmic Variable Stars (203), Intermediate Polars (407) – individual (Swift J1839-045)

1. INTRODUCTION

Cataclysmic Variables (CVs) are binary systems including a white dwarf (WD) accreting material from a companion, usually a main-sequence star, which is undergoing Roche Lobe overflow. An accretion disk can form if the magnetic field of the primary (the WD) is sufficiently small, i.e., $B \lesssim 10^6$ G (see e.g., Warner 1992, 1995; Coppejans 2016). Systems with field strengths below this threshold are known as nonmagnetic CVs, whereas the magnetic systems exceeding this field strength are divided into polars and intermediate polars (IPs). The difference between the latter two categories is that in the most magnetic WDs (polars), the Alfvén radius (R_A) extends to the L1 Lagrange point, which stops an accretion disk from forming, while in the lower B -field IPs an accretion disk can form between L1 and R_A . In addition, the magnetic field of polars induces a torque, which approximately synchronizes the WD spins to their orbital periods. In contrast, in IPs the weaker WD fields cannot synchronize spins with orbital periods and the WDs are in fact spun up by accretion torques (Cropper 1990; Patterson 1994; Wickramasinghe 2014).

In IPs, material at the inner edge of the disk is funnelled along the magnetic field lines towards the poles of the WD, forming a shock in the accretion column as it interacts with the WD atmosphere. Accretion from the inner edge of the disk results in azimuthally extended accretion curtains, akin to the auroral zones on Earth. During accretion, several emission mechanisms are at play; for a comprehensive review see Mukai (2017). At the shock front, thermal bremsstrahlung is the major contributor to the X-ray emission, while line cooling becomes increasingly important with lower temperatures at the post-shock (due to less-ionized accretion species). Most IP spectra have been fit with reasonable agreement to a bremsstrahlung model plus F_e lines; however, successful fits to wide-band, high quality X-ray spectra of IPs require more sophisticated models, including multi-temperature plasma models such as MKCFLOW, complex absorbers, and reflection (see, e.g., Lopes de Oliveira & Mukai 2019 and references therein). In a few so-called “soft” IPs, there is also a soft X-ray component (prevalent in polars) characterized by a blackbody with $T_{bb} \lesssim 100$ eV.

Non-magnetic CVs are most often discovered in the optical, via their variability or their spectral features. Even though the number of known non-magnetic CVs is increasing rapidly, thanks to Sloan Digital Sky Survey (SDSS) and to recent time-domain surveys, such as the All-Sky Automated Survey for Supernovae (ASAS-SN), our census is still only complete within the immediate Solar neighborhood. For example, Pala et al. (2020) constructed a volume-limited sample of CVs out to 150 pc, which includes SDSS, ASAS-SN, and Gaia discoveries, as well as one object discovered by an amateur astronomer. Magnetic CVs are, in general, the most X-ray luminous sub-class of CVs, and a large majority are discovered as X-ray sources. Polars generally are soft X-ray bright sources, so the current list of polars are dominated by *ROSAT*-discovered objects (see, e.g., Beuermann et al. 2020 and references therein). In contrast, most IPs are hard X-ray bright and soft X-ray faint (the latter being due to strong internal absorption). As a consequence a large majority of currently known IPs have been discovered with the *Swift* BAT and *INTEGRAL* hard X-ray surveys (de Martino et al. 2020). Each new X-ray survey has added to our census of, and our understanding of, magnetic CVs.

Here we present the discovery with the Niel Gehrels *Swift* Observatory Deep Galactic Plane Survey (DGPS; PI C. Kouveliotou) of Swift J183920.1–045350 (hereafter J1839); we also present our results of followup observations obtained with a multiwavelength campaign. J1839 is the second source we followed up in-depth within the scope of DGPS (Gorgone & Kouveliotou 2017). The DGPS is a *Swift* legacy program that covers the inner regions of the Milky Way (Phase I: $30^\circ > |\ell| > 10^\circ$ and $|b| < 0.5^\circ$). In section 2 we outline the methods used to extract and calibrate multiwavelength data. In section 3 we report on our sub-arcsecond localization, X-ray and IR spectroscopy, multiwavelength photometry, and timing analysis results. In section 4, we discuss our IP classification of the source. Finally, a summary of our work is presented in section 5.

2. OBSERVATIONS

J1839 was discovered on 2017, July 13 with the *Swift* DGPS with a 3.8 ks exposure, which revealed a 5.4σ detection above background (0.3 – 10 keV). However, it was not detected above 3σ in the single archival observation of the field with the *Swift* X-Ray Telescope (XRT) in 2013. Since this was a previously uncataloged source, we initiated a series of multi-wavelength observations to identify the optical counterpart and determine the source nature. We observed J1839 with our *Chandra* program Target of Opportunity (ToO) observation for localization as well as with our *XMM-Newton* and *NuSTAR* ToO programs to obtain X-ray spectra. We also obtained optical spectra with the Dual Imaging Spectrograph (DIS) at the Apache Point Observatory (APO) and with the Robert Stobie Spectrograph (RSS) at the Southern African Large Telescope (SALT), and performed optical photometry with the *Swift* Ultraviolet and Optical Telescope (UVOT) and the *XMM-Newton* Optical monitor (OM). A candidate counterpart was observed in archival data of the Zwicky Transient Facility (ZTF) in the g and r bands; the source flux evolution was tracked through two observing runs covering a total duration of ~ 700 days. Finally, we took high-speed photometry of the source

on 8 nights using the Sutherland High Speed Optical Camera (SHOC) camera on the South African Astronomical Observatory (SAAO) 1-m telescope. In addition we performed a brief polarimetric observation with the High speed PhotoPolarimeter (HIPPO). All observations are tabulated chronologically in Table 1 and described per wavelength range in detail below.

2.1. X-ray observations

2.1.1. Swift/X-Ray Telescope (XRT)

Count rates were determined using the XIMAGE routine `sosta`. We used source regions corresponding to an enclosed-energy fraction of 87%¹ and local background annuli outside these regions. The count rates were multiplied by a factor (calculated using the `xrtmkarf` command) to recover the full 100% of the enclosed-energy fraction. The source was discovered at a count rate of $1.5(3) \times 10^{-2}$ counts s^{-1} in photon counting (PC) mode. We also used data from the only archival observation taken in March 2013 with *Swift*/XRT in PC mode.

2.1.2. Chandra

We used one of our approved Targets of Opportunity to observe J1839 with the *Chandra* ACIS-I (Garmire et al. 2003) for 2.5 ks on 2018, November 9 (Obs. 9 in Tbl. 1). To prepare the data for analysis, we used routines `fluximage` and `dmcopy` from the `ciao v4.9` package. We determined the location of J1839 with sub-arcsecond accuracy (see section 3.1).

2.1.3. XMM-Newton

We used one of our approved Targets of Opportunity to observe J1839 for 26 ks on 2018, October 18 with the *XMM-Newton* (Jansen et al. 2001) EPIC cameras (PN; MOS1/2 - Strüder et al. 2001; Turner et al. 2001) in full frame imaging mode. To extract the data, we used the Science Analysis Software `SAS v.1.2` (Gabriel et al. 2004). We produced the final event files with `epchain` and `emchain` commands. We created circular source regions that contained 80% of the enclosed energy, with radii of 35'' and 25'' for the PN and MOS cameras, respectively². We extracted background regions of the same size from nearby, source-free regions. We filtered out times of high background in the 10–12 keV band and only included event patterns 0–4 for PN and 0–12 for both MOS lightcurves. Finally we corrected the event times to the Solar System barycenter using `barycen` with the source RA and DEC as found in our *Chandra* observation. We then filtered the master events file by energy to obtain data in three bands, namely 0.3 – 3.0 keV, 3.0 – 10.0 keV and 0.3 – 10.0 keV, for our timing and spectral analyses.

2.1.4. NuSTAR

We observed J1839 with *NuSTAR* (Harrison et al. 2013) and used `heasoft v.6.23` command `nuproducts` to produce level 3 data. We used the same circular source region (with a radius of 120'') centered on the *Chandra* location, in both focal plane modules. For the background, we used a circular region of the same radius from a source-free field. We barycenter-corrected the photon arrival times to the Solar System based on the *Chandra* position (see subsection 3.1). We truncated the *NuSTAR* data included in our fits at 20 keV, where the background flux started to dominate the source flux.

2.2. UV observations

Two of the X-ray satellites we used are equipped with ultraviolet (UV) monitors and provided contemporaneous UV and X-ray observations.

2.2.1. XMM-Newton/Optical Monitor

We observed J1839 with the UVM2 ($\lambda_{eff} = 231$ nm), UVW1 ($\lambda_{eff} = 291$ nm), and U ($\lambda_{eff} = 344$ nm) filters of the *XMM-Newton*/OM (Mason et al. 2001). We used the `SAS` command `omichain` to process the data, which aggregated a final list of uniquely detected sources for each filter and produced photometric measurements for each source.

¹ This leads to slightly different region sizes due to the energy dependence of the Point Spread Function.

² See § 3.2.1.1 of the XMM Users Handbook <https://heasarc.nasa.gov/docs/xmm/uhb/onaxisxraypsf.html>

2.2.2. *Swift/Ultraviolet-Optical Telescope*

The *Swift*/UVOT (Roming et al. 2005) is identical to the *XMM-Newton*/OM³, with slightly different filter throughput. We observed J1839 with the UVM2 ($\lambda_{eff} = 225$ nm), UVW1 ($\lambda_{eff} = 268$ nm), and U ($\lambda_{eff} = 352$ nm) filters. To process these data, we used the level 3 stacked sky images produced by the HEASARC and used the HEASOFT command `uvotsource` with a $3''$ radius region, centered on the *Chandra* location. A nearby source-free region of radius $16''$ was extracted as a background reference.

2.3. *Optical observations*

2.3.1. *Zwicky Transient Facility photometry*

We retrieved publicly-available photometry of J1839 from the Zwicky Transient Facility (ZTF; Bellm et al. 2019; Graham et al. 2019) Data Release 4⁴. ZTF observed J1839 sporadically between 2018, March 28 to 2020, June 28, a total of 135 times with the ZTF g band filter and 241 times with the ZTF r band filter. PSF photometry was automatically extracted using the pipeline described in Masci et al. (2019). We found one source in ZTF data within the *Chandra* error circle.

2.3.2. *Southern African Large Telescope (SALT) spectroscopy*

Spectroscopy of J1839 was undertaken with the Southern African Large Telescope (SALT; Buckley et al. 2006) during one night in 2019 and six in 2020 (see Table 1). The Robert Stobie Spectrograph (RSS; Burgh et al. 2003) was used, initially with the PG900 VPH grating, covering the region 4060–7120 Å at a mean resolution of 4.7 Å with a $1.5''$ slit width. All exposures were 1800 s. The last three observations utilized the PG1800 VPH grating, covering 5800–7100 Å at a resolution of 2.4 Å, also with a $1.5''$ slit. Six repeat 500 s exposures were taken. For all observations, wavelength calibration lamp exposures were taken immediately following the observations on each night.

The spectra were reduced using the PySALT package (Crawford et al. 2010)⁵, which does bias, gain and amplifier cross-talk corrections, mosaics the three CCDs and applies cosmetic corrections. Object extraction, wavelength calibration and background subtraction were all done using standard IRAF⁶ routines, as was the relative flux calibration.

2.3.3. *South African Astronomical Observatory (SAAO) photometry and photopolarimetry*

Time series photometry of J1839 was undertaken on 8 nights (see Table 1) using the SAAO 1 m telescope⁷ with the Sutherland High speed Optical Camera (SHOC) CCD camera. SHOC uses an Andor iXon888 frame transfer EM-CCD frame camera, with 1024×1024 pixels (Coppejans et al. 2013), in conventional (non electron-multiplying; EM) mode. All observations were done without a filter (i.e., ‘white light’); an exposure time of 30 sec was used.

Reduction of the CCD images included subtraction of median bias and flat-field correction using median-combined frames from exposures of the twilight sky. Aperture-corrected photometry was used to extract the light curves of all stars in the calibrated science images and differential photometry was performed using several local reference stars.

Time resolved filterless all-Stokes polarimetry of J1839 was obtained on 2020, July 15, over a period of ~ 1400 s with the HIPPO photopolarimeter (Potter et al. 2010).

2.4. *Radio observations*

2.5. *Karl G. Jansky Very Large Array (VLA)*

We were allocated 6 hours of Director’s Discretionary Time (DDT) to observe J1839 with the Karl G. Jansky Very Large Array (VLA) in the X-band (8–12 GHz). X-band was chosen to maximize sensitivity, while decreasing Radio Frequency Interference (RFI). Despite the band selection, both observations were significantly affected by RFI, and we removed bands above 10.8 GHz to mitigate spurious signals. All VLA observations used the 3-bit continuum mode with 4 GHz of continuous bandwidth. In our first observation (Obs. 15 in Table 1), J1839 was observed with 27 antennas. In Obs. 16 and 17, 19 and 25 antennae were used, respectively. Throughout all of our observations, we used J1832-1035 as the complex gain calibrator. We used 3C48 (J0137+3309) as the flux density and bandpass calibrator. We note that 3C48 was known to undergo flaring activity at the time of the observation, causing the absolute flux density estimates to be uncertain to $\sim 10\%$.

³ *Swift*/UVOT modules are the flight spares of the *XMM-Newton*/OM., see https://swift.gsfc.nasa.gov/about_swift/uvot_desc.html

⁴ <https://www.ztf.caltech.edu/page/dr4>

⁵ <https://astronomers.salt.ac.za/software/pysalt-documentation/>

⁶ <https://iraf.noao.edu/>

⁷ See <https://www.sao.ac.za/astronomers/telescopes-1-0m/> for telescope details.

Table 1. Multi-wavelength Observations of Swift J183920.1–045350 are enumerated in chronological order.

Obs.	ID	Telescope	Instrument/Mode	Start Time [UT] [dd Mmm yyyy hh:mm]	Duration [ks]
1.	00044416001	<i>Swift</i>	XRT/PC + UVOT	21 Mar. 2013 06:59	0.5
2.	00087393001	<i>Swift</i>	XRT/PC + UVOT	13 Jul. 2017 06:02	3.8
3.	00087393002	<i>Swift</i>	XRT/PC + UVOT	14 Nov. 2017 02:42	1.1
4.	00010900001	<i>Swift</i>	XRT/PC + UVOT	01 Oct. 2018 17:09	1.0
5.	0821860201	<i>XMM</i>	PN + MOS + OM	18 Oct. 2018 11:27	26.0
6.	30360002002	<i>NuSTAR</i>	FPMA/B	02 Nov. 2018 08:04	40.8
7.	00088814001	<i>Swift</i>	XRT/PC + UVOT	02 Nov. 2018 12:30	1.4
8.	00088814002	<i>Swift</i>	XRT/WT + UVOT	08 Nov. 2018 13:34	0.6
9.	20335	<i>Chandra</i>	ACIS-I	09 Nov. 2018 08:49	2.5
10.	00087393003	<i>Swift</i>	XRT/PC + UVOT	07 Jul. 2019 21:29	0.2
11.	-	APO	DIS/red	13 Jul. 2019 05:54	3.6
12.	-	SALT	RSS PG900	22 Jul. 2019 19:23	1.8
13.	-	SAAO 1-m	SHOC, Clear	9 Oct. 2019	7.3
14.	-	SAAO 1-m	SHOC, Clear	13 Oct. 2019	7.2
15.	19B-340	VLA	X-band, D config.	31 Dec. 2019 19:16	7.3
16.	19B-340	VLA	X-band, D config.	03 Jan. 2020 19:14	7.3
17.	19B-340	VLA	X-band, D config.	04 Jan. 2020 19:28	7.2
18.	-	ZTF	r-band & g-band	continuous	-
19.	-	SAAO 1-m	SHOC, Clear	22 May 2020 23:16	15.3
20.	-	SAAO 1-m	SHOC, Clear	15 Jul. 2020 20:14	6.1
21.	-	SAAO 1.9-m	HIPPO, Clear	16 Jul. 2020 00:14	1.4
22.	-	SAAO 1-m	SHOC, Clear	16 Jul. 2020 18:31	25.3
23.	-	SAAO 1-m	SHOC, Clear	21 Jul. 2020 19:03	14.9
24.	-	SALT	RSS PG900	21 Jul. 2020 19:45	1.8
25.	-	SALT	RSS PG900	23 Jul. 2020 19:17	1.8
26.	-	SALT	RSS PG900	24 Jul. 2020 18:58	1.8
27.	-	SALT	RSS PG1800	13 Aug. 2020 21:18	0.5 × 6
28.	-	SAAO 1-m	SHOC, Clear	19 Aug. 2020	12.0
29.	-	SAAO 1-m	SHOC, Clear	22 Aug. 2020	14.6
30.	-	SALT	RSS PG1800	22 Aug. 2020 20:33	0.5 × 6
31.	-	SALT	RSS PG1800	19 Sep. 2020 18:54	0.5 × 6

NOTE— ★ No HR calculation possible (source upper limit), † Source outside field of view or in damaged pixel area, - Outside of the 0.3 – 10.0 keV soft X-ray window.

3. RESULTS

Here we describe the source localization, and the temporal and spectral analyses results. Contrary to the previous section, which was organized by wavelength, here subsections are organized according to the type of analysis performed. A comprehensive summary of source characteristics can be found in the final table at the discussion part of this paper (Table 5).

3.1. Localization, Distance, and Proper Motion

We determined the *Chandra* location of J1839 using `wavdetect` with `ciao v4.9` (Obs. 9 in Tbl. 1). We found one source at R.A. $18^h39^m19^s.98$, decl. $-04^\circ 53' 53.1''$ (J2000) with a positional uncertainty of $0.8''$ (90% confidence, systematic error) within the astrometrically-corrected XRT-UVOT position (ACP). The latter was calculated using the method described in [Evans et al. \(2014\)](#). Fig. 1 shows the *Chandra* field with the XRT/ACP error circle (green) superposed on the *Chandra* source (red). The XRT/ACP location center is offset from the *Chandra* location by $0.683''$.

Further, we searched the Gaia DR2 data [Gaia Collaboration et al. \(2018a\)](#) within the *Chandra* uncertainty region. We identified one source, Gaia DR2 4256603449854150016 ($G_{\text{Gaia}}=18.5$), which is offset from the *Chandra* location centroid by $0.193''$ (black cross, Fig. 1). Taking into account the significantly larger *Swift*/XRT point spread function, we conclude that the *Chandra* and Gaia sources are indeed the counterparts of J1839.

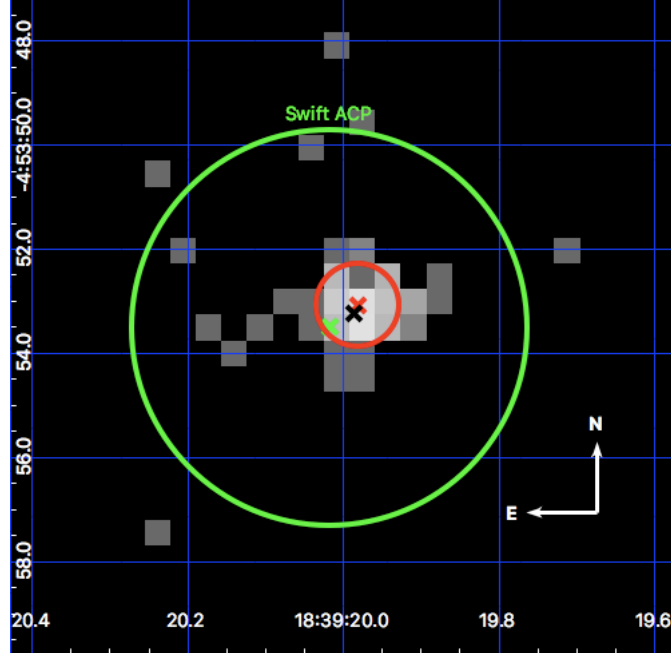


Figure 1. *Chandra* image (Obs.9 from Tbl.1) with the *wadetect* position and pointing uncertainty ($\sim 0.8''$) in red, the XRT/ACP position with a 90% uncertainty circle from Obs.2 (green), and the Gaia location (black x, uncertainty of $\sim 0.2 \text{ mas}$). The image is binned at the native plate scale of *Chandra*, 1 pixel $\sim 0.5''$.

Finally, we adopt the distance and proper motion of the Gaia source for J1839 for the remaining analysis. The former is estimated to be $2.26^{+1.93}_{-0.83}$ kpc (68% confidence; [Bailer-Jones et al. 2018](#)). The proper motion is $\mu_{\alpha}, \mu_{\delta} = -1.1 \pm 0.4, -2.6 \pm 0.4 \text{ mas yr}^{-1}$, where the uncertainties are expressed as standard errors by the [Gaia Collaboration et al. \(2018b\)](#). In Section §3.4 we discuss the optical and IR photometry results within the source distance context.

3.2. Spectroscopy

We observed J1839 in three different wavebands: in the X-rays (0.5–20 keV), and the optical between 4000–7000 Å and 5500–9000 Å. Below we describe our spectral analyses.

3.2.1. X-ray Spectrum

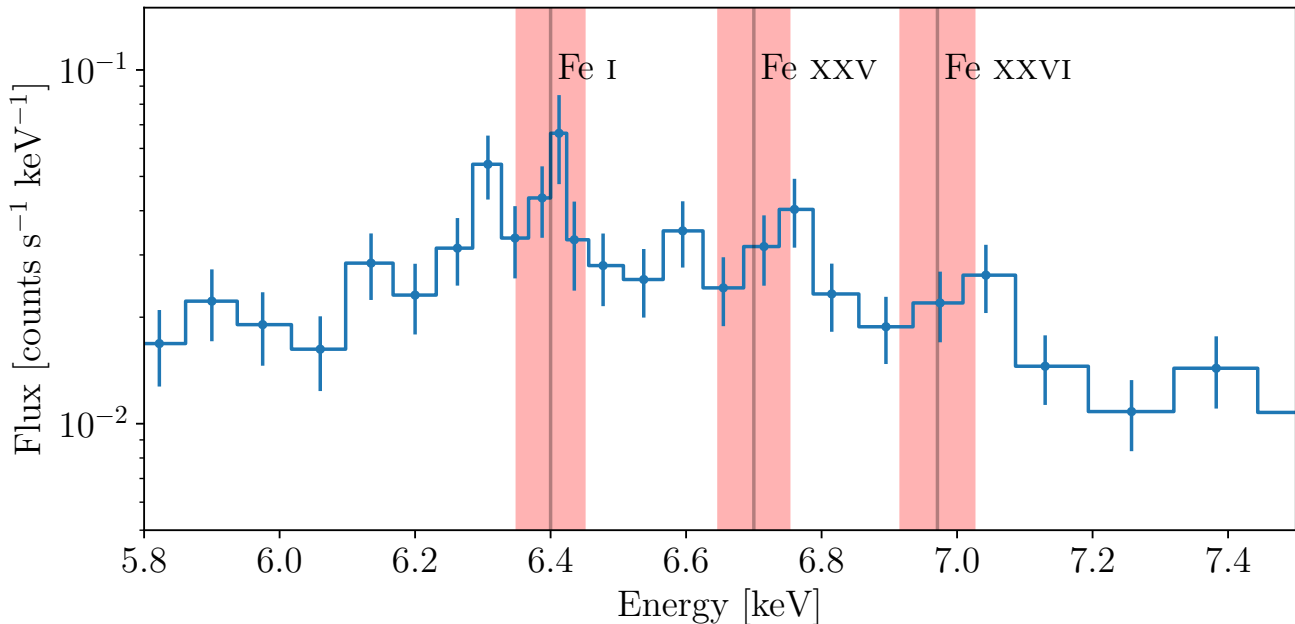


Figure 2. Spectral lines as observed with *XMM-Newton* EPIC PN are shown with the rest energies of the Fe species. Red shaded regions show possible energy shifts in the lines if the source has a velocity along the line of sight of $|v_r| \leq 2.34 \times 10^3$ km s $^{-1}$.

We used the *NuSTAR* and *XMM-Newton* data for our spectral fits, as these were the highest quality data sets. We first visually inspected the data, and found deviation from a smooth spectrum in the 6 – 7 keV range. This is most significant in the PN spectrum (Fig. 2).

The *XMM-Newton* and *NuSTAR* spectra were first fitted separately with XSPEC with an absorbed powerlaw (PL) to identify general broadband spectral properties. A constant prefactor was used to allow for simultaneous fitting across all EPIC cameras (*XMM-Newton*) or focal plane modules (*NuSTAR*). The prefactor was frozen to 1 in the first spectrum in the group, and all others were left free to vary. To check for spectral evolution, we first fit both datasets with a PL in their overlapping spectral range (3 – 10 keV); these fits yielded PL indices of $\Gamma = 1.3_{-0.2}^{+0.3}$ in the *XMM-Newton* data (1σ uncertainties) and $\Gamma = 2.2 \pm 0.2$ in the *NuSTAR* data (1σ uncertainties). Therefore, J1839 appeared to have varied significantly over the ~ 15 day period between observations 5 and 6 in Tbl. 1. However, large positive residuals remained in the 6 – 7 keV range, which encompasses the F_e line complex (right middle panel of Fig. 3). We added a Gaussian component to account for the F_e lines. We refer to this absorbed PL plus Gaussian as Model 1. This model provided a good fit to both individual spectra with a reduced $\chi^2 = 167.33/208 = 0.84$ for *XMM-Newton* and $\chi^2 = 171.78/191 = 0.93$ for the *NuSTAR* spectrum. All best-fit parameter values agreed within 1σ in both instruments, therefore, we proceeded in fitting the two data sets together.

We also used a prefactor for each spectrum in the joint fits with Model 1. The prefactors varied less than 10 percent for all *XMM-Newton* instruments; we chose to freeze the PN factor to 1. For *NuSTAR*, the prefactors were best fit at 1.43 and 1.23 for Focal Plane Module (FPM) A and B, respectively; the prefactor for FPMA is $\geq 16\%$ greater than FPMB for all models tested. This discrepancy could be due to a rip in the multi-layer insulation recently reported by Madsen et al. (2020).

Motivated by the optical spectra that suggested that J1839 was a CV (see below), and quite possibly an intermediate polar (IP), we introduced Model 2. Model 2 comprises two absorbing columns (tbabs for interstellar medium and pwab (Done & Magdziarz 1998) for a local partial covering absorber) with a broadband, isobaric cooling flow component (mkcflow) and a Gaussian for the ~ 6.4 keV spectral line. While fitting Model 2, the nHmin parameter of pwab was frozen to 1.0×10^{15} cm $^{-2}$ and the lowT parameter was frozen to 0.0808 keV. The redshift parameter of mkcflow was frozen to the minimum 1.0×10^{-7} , given the Gaia source distance of ~ 2 kpc. We show the best fit result in the left panel of Fig. 3. Similar prefactor values were found for both Model 1 and 2.

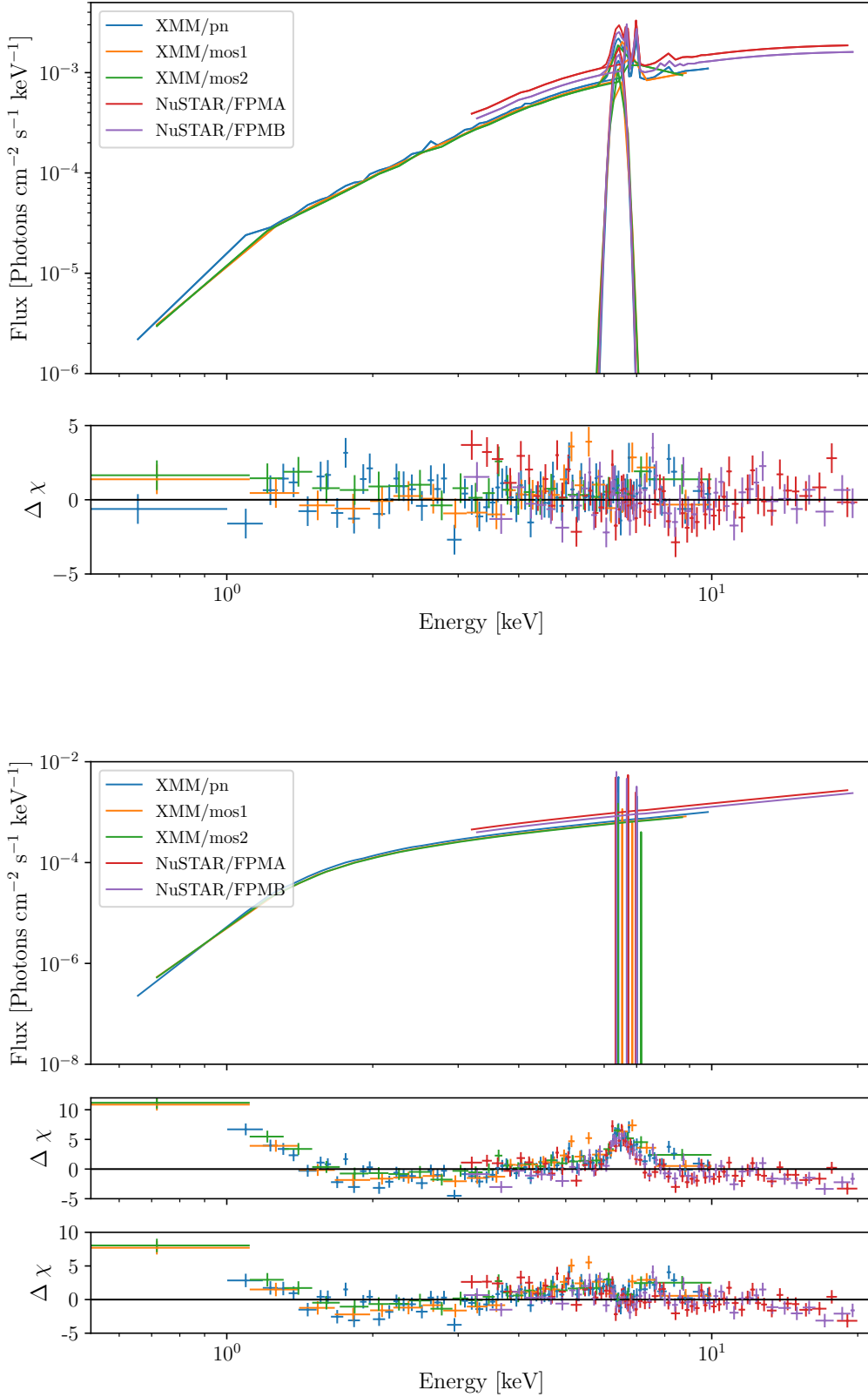


Figure 3. XMM-Newton and NuSTAR spectral models are shown in the upper panels with the data residuals in the lower panel. (*Top*) Model 2 in the top panel and residuals below it (*Bottom*) Model 3 with associated residuals (top and bottom subpanels) as described in Tbl. 2 compared to `constant*tbabs(powerlaw)` residuals in the middle subpanel. Data are binned to a minimum of 5σ significance for visual clarity.

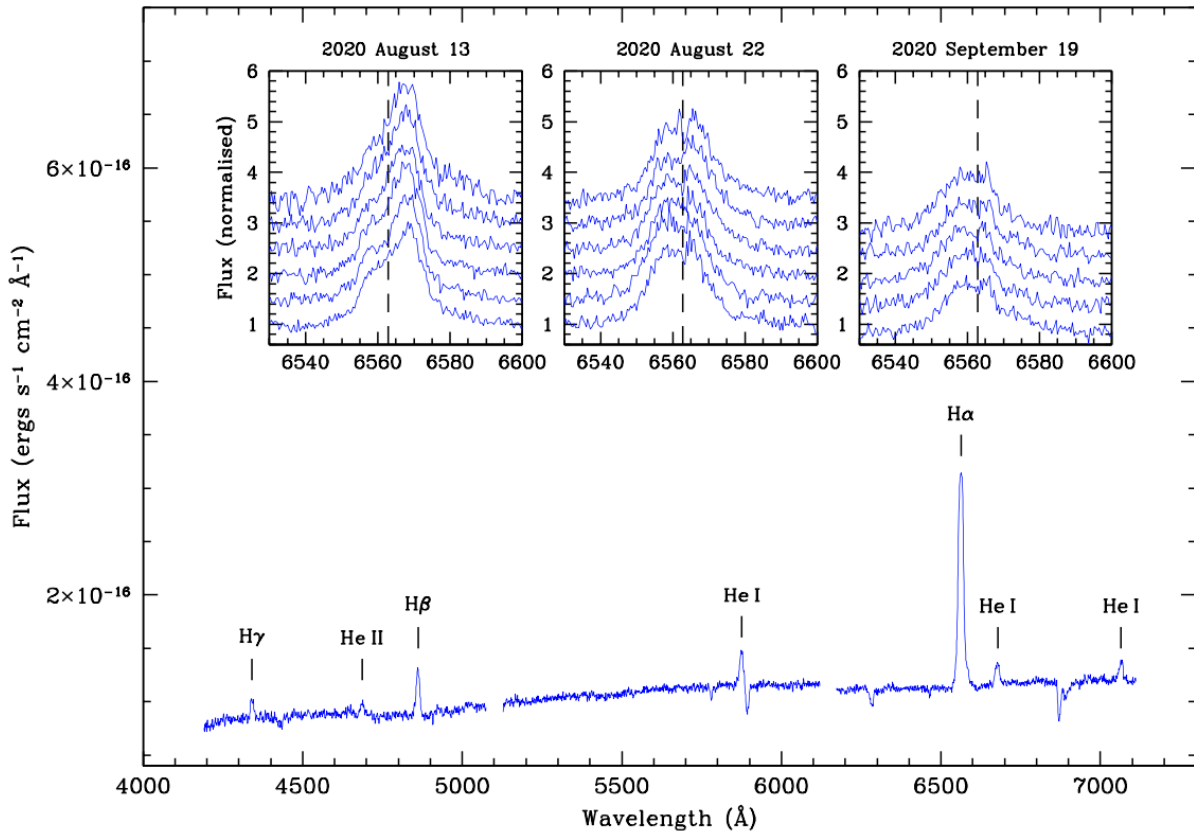


Figure 4. The average SALT RSS spectrum of J1839 covering the wavelength range of 4190 to 7100 Å. The main emission lines are marked and labelled. The insets show the varying H α emission line profiles as observed at higher spectral resolution (PG1800) on SALT on three different days; each sequence shows a series of consecutive 500-s spectra (first to last: bottom to top). The vertical dashed line in the insets indicates the rest wavelength of H α .

Finally, we fit the data with an absorbed PL with three Gaussians (referred to as Model 3), corresponding to the ionized F_e lines typically seen in CVs (Hellier et al. 1998; Ezuka & Ishida 1999; Hellier & Mukai 2004), and also suggested by the PN spectrum (Fig. 2). These narrow line components were frozen at central energies 6.4, 6.7, and 6.97 keV and their standard deviations were frozen at 0.0 keV (one spectral bin width). This model is highlighted in the top right panel of Fig. 3, with associated residuals shown in the bottom right. We compare all three models in Section 4.

To obtain the source fluxes with each of these models, we froze the model normalizations and added a `cflux` component to the spectral model to measure unabsorbed flux. We set the energy band from 0.3 keV to 20.0 keV. The resulting values are reported in the last row for each model in Tbl. 2. For spectral Model 2, we calculate a luminosity of $L_{0.3-20.0} = (2.44_{-0.85}^{+2.43}) \times 10^{33}$ erg s $^{-1}$, based on the unabsorbed flux and the Gaia counterpart distance. The flux and distance fractional uncertainties were added in quadrature; the distance uncertainty contributed to the large upper uncertainty of the luminosity.

3.2.2. Optical spectra

Fig. 4 shows the averaged flux-calibrated SALT RSS spectrum of J1839, where we combined the two highest signal-to-noise spectra obtained on 2020, July 21 and 23, respectively. The spectrum is characterised by strong H I (Balmer), He I and He II emission lines, on top of a continuum which rises to the red. This spectrum establishes J1839 as a likely CV. The H α emission is the strongest and we also see both the high excitation He II 4686Å and Bowen fluorescence (4640 – 4660Å) lines, both a common feature seen in magnetic CVs as a result of the ionizing soft X-ray emission

Table 2. Best fit parameters for Models 1, 2, and 3 (see NOTE)

Model	parameter	value $\pm 90\%$ confidence	unit	
1. PL + Gaussian	TBabs: N_{H}	$1.58^{+0.31}_{-0.25}$	10^{22} cm^{-2}	
	Cstat = 2308	PhoIndex	$1.02^{+0.07}_{-0.07}$	
	2812 d.o.f	PL norm	$1.06^{+0.17}_{-0.14}$	10^{-4}
	or	LineE	$6.50^{+0.05}_{-0.07}$	keV
	$\chi^2 = 2518.91$	Gaussian Sigma	$0.45^{+0.16}_{-0.09}$	keV
	2812 d.o.f.	gaussian: norm	$2.94^{+0.55}_{-0.41}$	10^{-5}
	$\chi^2_{\text{red}} = 0.90$	unab. Flux $_{0.3-20.0}$	$2.87^{+0.16}_{-0.15}$	$10^{-12} \text{ erg s}^{-1} \text{ cm}^{-2}$
2. mkcflow + Gaussian	Tbabs: N_{H}	$0.33^{+0.18}_{-0.16}$	10^{22} cm^{-2}	
	Cstat = 2144	pwab: nHmax	$29.05^{+21.07}_{-9.12}$	10^{22} cm^{-2}
	2809 d.o.f.	pwab: beta	$-0.38^{+0.08}_{-0.07}$	
	or	mkcflow: highT	$63.18^{+16.72}_{-26.52}$	keV
	$\chi^2 = 2350$	mkcflow: Abundanc	$1.69^{+1.07}_{-0.90}$	
	2809 d.o.f.	mkcflow: norm	$8.85^{+8.39}_{-2.58}$	10^{-12}
	$\chi^2_{\text{red}} = 0.84$	gaussian: LineE	$6.41^{+0.08}_{-0.05}$	keV
		gaussian: Sigma	$13.83^{+9.78}_{-8.03}$	10^{-2} keV
		gaussian: norm	$1.23^{+0.44}_{-0.29}$	10^{-5}
		unab. Flux $_{0.3-20.0}$	$4.31^{+0.47}_{-0.39}$	$10^{-12} \text{ erg s}^{-1} \text{ cm}^{-2}$
3. PL + 3 Gaussians	TBabs: N_{H}	$1.89^{+0.31}_{-0.27}$	10^{22} cm^{-2}	
	Cstat = 2335	powerlaw: PhoIndex	$1.08^{+0.07}_{-0.07}$	
	2812 d.o.f	powerlaw: norm	$1.25^{+0.18}_{-0.15}$	10^{-4}
		gaussian: LineE	6.40	keV
	or	gaussian: Sigma	0.0	keV
		gaussian: norm	$1.02^{+0.15}_{-0.14}$	10^{-5}
	$\chi^2 = 2537$	gaussian: LineE	6.70	keV
		gaussian: Sigma	0.0	keV
	2812 d.o.f.	gaussian: norm	$6.75^{+1.48}_{-1.40}$	10^{-6}
		gaussian: LineE	6.97	keV
		gaussian: Sigma	0.0	keV
	$\chi^2_{\text{red}} = 0.90$	gaussian: norm	$4.30^{+1.26}_{-1.20}$	10^{-6}
		unab. Flux $_{0.3-20.0}$	$2.94^{+0.16}_{-0.16}$	$10^{-12} \text{ erg s}^{-1} \text{ cm}^{-2}$

NOTE—Model 1: `constant*tbabs(powerlaw+gaussian)`Model 2: `constant*phabs*pwab(mkcflow + gaussian)`Model 3: `constant*Tbabs(powerlaw + gaussian + gaussian + gaussian)`.

Brackets on parameters denote that the uncertainty extends to the upper ([]) or lower limit (]) of the model parameter allowed by XSPEC.

(McClintock et al. 1975; Mukai 2017). Whereas the He II 4686Å line can be brighter than the neighboring H β line in polars, it is typically weaker in intermediate polars.

Given the strength of the H α line, we obtained higher resolution SALT spectra (using the PG1800 grating on RSS) on three different nights in 2020 August - September (Obs. 27, 30 & 31 in Tbl. 1). The inserts in Fig. 4 show the varying H α profiles. From night to night there is clear variability in the line profile but unfortunately the coverage of the high resolution spectra is too sparse to look for coherent variability on the time scale of a possible orbital period.

3.3. Timing

We searched the *XMM-Newton*, *NuSTAR*, and *SAAO* data for periodicities. For *XMM-Newton* we created a Z_1^2 statistic (Buccheri et al. 1983), in the 0.3 – 10.0 keV band of EPIC PN. The resulting power spectrum showed a maximum at $(2.228 \pm 0.004) \times 10^{-3}$ Hz, i.e., a period of 448.7 ± 0.3 s. To search for periodicities in the *NuSTAR* data, we corrected the photon arrival times to the Solar System barycenter using the HEASOFT v.6.23 command

Table 3. Best fit parameters for the pulse profile model $C + A \sin(2\pi\phi) + B \cos(2\pi\phi)$ are shown for energy bands from observations 5 and 6. Errors are at the 68% confidence interval.

Parameter [units]	Combined XMM EPICs			Combined NuSTAR FPMs		
	0.3–3.0 keV	3.0–10.0 keV	0.3–10.0 keV	3.0–10.0 keV	10.0–20.0 keV	3.0–20 keV
Constant, C [cts]	151.20 ± 3.45	275.40 ± 3.11	426.60 ± 5.22	428.20 ± 5.73	161.60 ± 4.49	588.50 ± 5.43
Amplitude A [cts]	-30.82 ± 4.87	-17.84 ± 4.40	-48.66 ± 7.38	9.67 ± 8.11	-6.53 ± 6.35	2.19 ± 7.68
Amplitude B [cts]	-13.30 ± 4.87	-25.30 ± 4.40	-38.60 ± 7.38	-48.13 ± 8.11	-5.80 ± 6.35	-54.50 ± 7.68
Pulsed Fraction [%]	15.0 ± 3.0	7.6 ± 2.3	10.0 ± 1.7	7.9 ± 2.4	†	6.4 ± 1.9
χ^2 (χ^2_{RED} ; 7 DOF)	5.37 (0.77)	2.42 (0.35)	4.53 (0.65)	4.24 (0.61)	6.63 (0.95)	2.76 (0.39)

NOTE—† The pulsed fraction could not be determined, due to a low number of pulsed counts.

hdaxbary. We set the location to the source centroid measured with *Chandra*. We extracted source events from the 80% Enclosed Energy Fraction (EEF) radius of 75'' for the most conservative 3 – 4.5 keV energy range (An et al. 2014, Fig. 5). A Lomb-Scargle frequency analysis of the *NuSTAR* data (FPM A and B) shows a peak at $f_{NuSTAR1} = (2.2268 \pm 0.0016) \times 10^{-3}$ Hz, consistent with the peak frequencies observed in the XMM observations, but with considerably better accuracy. The resulting power spectrum is shown in the lower panel of Fig. 6. The X-ray period is 449.1 ± 0.3 s. A Z_1^2 test in the combined FPMA and FPMB *NuSTAR* data within a 3 – 30 keV range, found a 5σ peak at $f_{NuSTAR2} = (2.2239 \pm 0.0017) \times 10^{-3}$ Hz, corresponding to an X-ray period of 449.7 ± 0.6 s. Given that the above period values are all consistent within $\sim 1\sigma$, and also taking into account the extended energy range of the latter estimate, as well as the significant jitter associated with white dwarf timing, we adopt the latter as the spin period of J1839, as it is far too short to be the orbital period of a non-degenerate hydrogen-rich CV. Littlefield et al. (2016) demonstrated a pronounced (almost 0.2 cycle) phase shift in the optical spin pulse of FO Aqr when it entered a low state (see their Figure 5). J1839 may also be demonstrating phase jitters of up to 0.1 cycle in total range during the source high state in figures 5 and 6, which can be plausibly interpreted as due to accretion rate changes. While phase jitters have not been directly observed in X-rays, Hellier (1997) observed orbital phase shift in the eclipse egress timing in XY Ari, which they interpret as random shifts in the position of the accreting spots in that IP.

We then folded all three EPIC camera lightcurves with the 449.7 s period, (Fig. 5) using the `fold_events` command in Python package STINGRAY v.0.1 (Huppenkothen et al. 2019). The folded pulse profiles were fit with the first harmonic function of Bildsten et al. (1997), i.e., $A \sin(2\pi\phi) + B \cos(2\pi\phi) + C$, with parameters A, B, and C free to vary. The resulting best-fit parameters, their standard deviations (σ_X), and χ^2 fit statistic are reported in Tbl. 3.

We calculated the root mean square pulsed fraction (PF_{RMS}) using Eq. 1.

$$PF_{RMS} = C^{-1} \sqrt{0.5 \times (A^2 + B^2 - \sigma_A^2 - \sigma_B^2)} \quad (1)$$

To calculate the uncertainty on PF_{RMS} , we performed 10^4 simulations of the pulse profile. In each simulation we created a synthetic pulse profile by drawing data points from Gaussian distributions. The Gaussian was unique to each phase bin, with a mean equal to the bin value and standard deviation equal to the bin uncertainty. Each synthetic pulse profile was fit with the same model described above, and the pulsed fraction was recorded. After all simulations were complete, we created a histogram of PF_{RMS} values, which was fit with a Gaussian. The standard deviation of the best-fit Gaussian was taken to be the uncertainty of PF_{RMS} . We used the same methods as in the *XMM-Newton* data to plot and determine the pulsed fraction in the *NuSTAR* data.

The 2020 SAAO high speed photometry (see Sect. 3.4.1) was used to search for coherent short-period optical modulations. We employed the generalized Lomb-Scargle period search as implemented in VARTOOLS (Hartman & Bakos 2016) to identify peak frequencies in the optical data. The top panel of Fig. 6 shows the Lomb-Scargle periodogram of the SAAO photometry between 1.2 and 3.2 mHz (left side), and a zoomed in view between 2.1 and 2.3 mHz (right side). A clear peak is identified at 2.17441×10^{-3} Hz with a formal false alarm probability of 1.1×10^{-14} , which we associate with the beat frequency ($\omega - \Omega$), where ω is the spin frequency determined from the X-ray data, and Ω is the inferred orbital frequency. The optical beat frequency corresponds to a period of 459.89 ± 0.13 s. When interpreted using the 449.7 ± 0.3 X-ray spin period, this implies that the inferred orbital period is 5.6 ± 0.6 hr, where the error is dominated by the uncertainty in the X-ray spin frequency.

After pre-whitening the optical data with the beat frequency, a small residual remains at the location of the X-ray spin frequency. This is shown in the middle panels of Fig. 6. The zoomed in view (middle-right panel) shows a

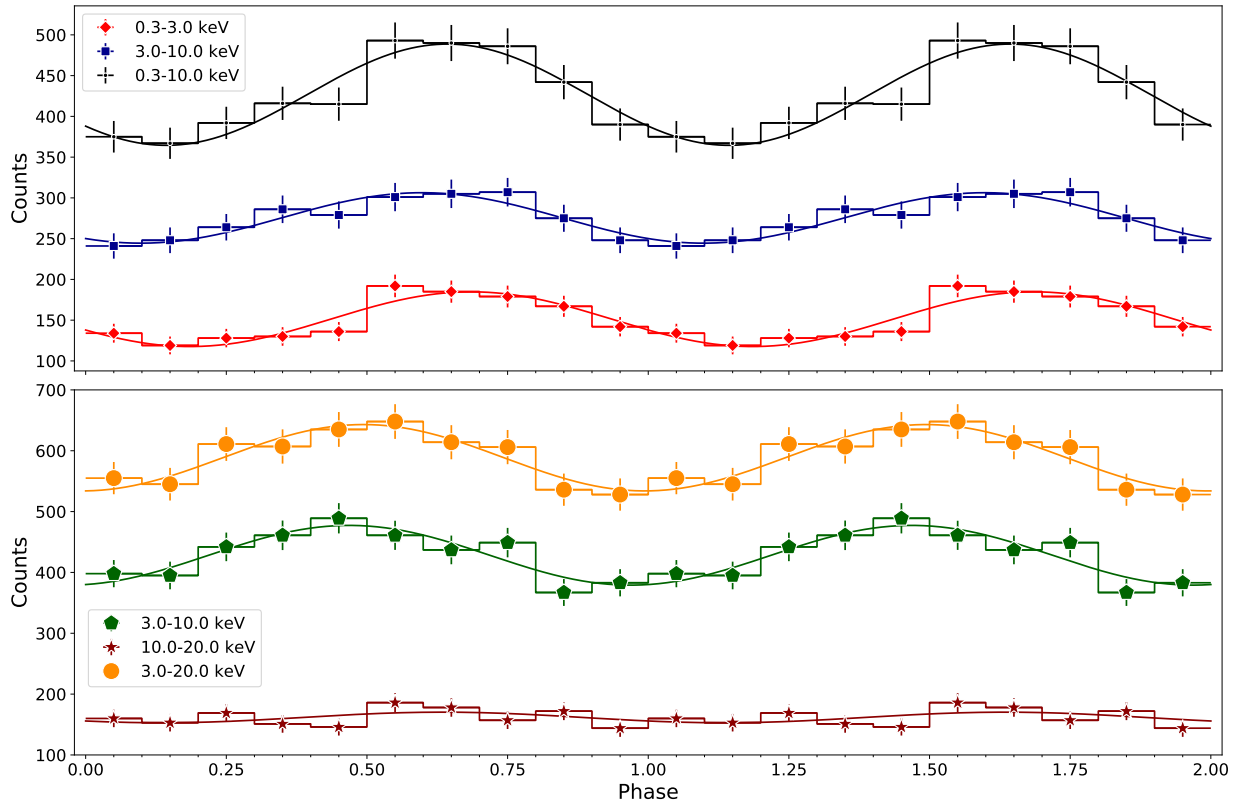


Figure 5. Pulse profile using (*Top:*) the combined *XMM-Newton* EPIC cameras in three energy bands from Obs. 5 and (*Bottom:*) the combined focal plane modules of *NuSTAR* in three energy bands. The data plotted are repeated over two full periods for visual clarity, in bins of 0.1 period ~ 44.97 s.

number of alias peaks around the X-ray spin frequency (vertical dashed line), making it hard to improve on the exact determination of the spin frequency. Nonetheless, there is clearly some power in the optical Lomb-Scargle periodogram at the spin frequency. The simultaneous presence of spin and beat periods in the optical is typical of IPs (Warner 1986; Pretorius 2009; Littlefield et al. 2016). The relative strength of the beat modulation indicates that optical pulses are dominated by the X-rays reprocessed by structures fixed in the binary frame, such as the secondary or the bright spot where the accretion stream interacts with the accretion disk.

In general, the SAAO photometric runs are less than 5 hr in length, with only one long observing run of 7 hrs (Obs. 22). This, together with the complex alias structure in the power spectrum, dominated by the ~ 5 d sampling, makes it hard to reliably identify low frequency orbital modulations in the SAAO data. However, two period maxima are seen in the power spectrum, close to the purported $\sim 5.6 \pm 0.3$ h orbital modulation, at 5.25 and 5.49 d. We searched for longer periods using the more extensive coverage ZTF photometry of J1839 in the r-band and found a peak in the power spectrum at 5.448 h, consistent with the predicted orbital period, although similar power is seen at several of the 1 cycle d^{-1} aliases either side.

3.4. Photometry

We searched with the VOSA tool (Bayo et al. 2008) for archival data within $2''$ of the *Chandra* position of J1839. We found a candidate counterpart in the Panoramic Survey Telescope and Rapid Response System (Pan-STARRS, Chambers et al. 2016) g, r, i, z, and y bands, PSO J183919.988–045353.099 (PS1 identifier 102122798332882651), which is $0.178''$ offset from J1839. We then searched the Gaia data release 2 (Gaia Collaboration et al. 2018a) and found G, G_{BP} , and G_{RP} magnitudes of the source Gaia DR2 4256603449854150016, which is offset by $0.193''$ from the *Chandra* position of J1839 (see also Fig. 1).

3.4.1. SAAO high speed photometry

Fig. 7 shows the SAAO high speed photometry of J1839 for five of the longest observing runs in 2020. The data were obtained in white light (unfiltered) and calibrated using Pan-STARRS r-band photometry of reference stars in the field. Such a calibration is only accurate to ~ 0.1 mag, see discussion in Coppejans et al. (2014). J1839 is around 18.4 mag during these observations. In Fig. 7, Obs. 19 is shown at the correct brightness and subsequent runs have been offset for display purposes. The light curves show the characteristic variability of a CV. In parts of the light curve, the optical modulation at 459.89 s is clearly visible by eye, e.g in Obs. 29 where we have marked the peaks of the beat period by small vertical dashes in Fig. 7. No clear orbital modulation on time scales of ~ 5 hr is visible in the light curves.

3.4.2. Optical polarization

The results of the HIPPO photopolarimetry of J1839 are presented in Fig. 8. No circular polarization, typical of magnetic CVs, particularly polars, was detected ($\langle V/I \rangle = 0.01\%$ S.D. = 0.46%). Since most IPs do not show detectable polarization, this is not surprising. The mean linear polarization value was $\langle p \rangle = 1.47\%$ with S.D. = 0.67%, with no obvious variability. This is consistent with an interstellar origin. The position angle of the linear polarization is $\theta = 95^\circ \pm 12^\circ$, consistent with an ISM origin.

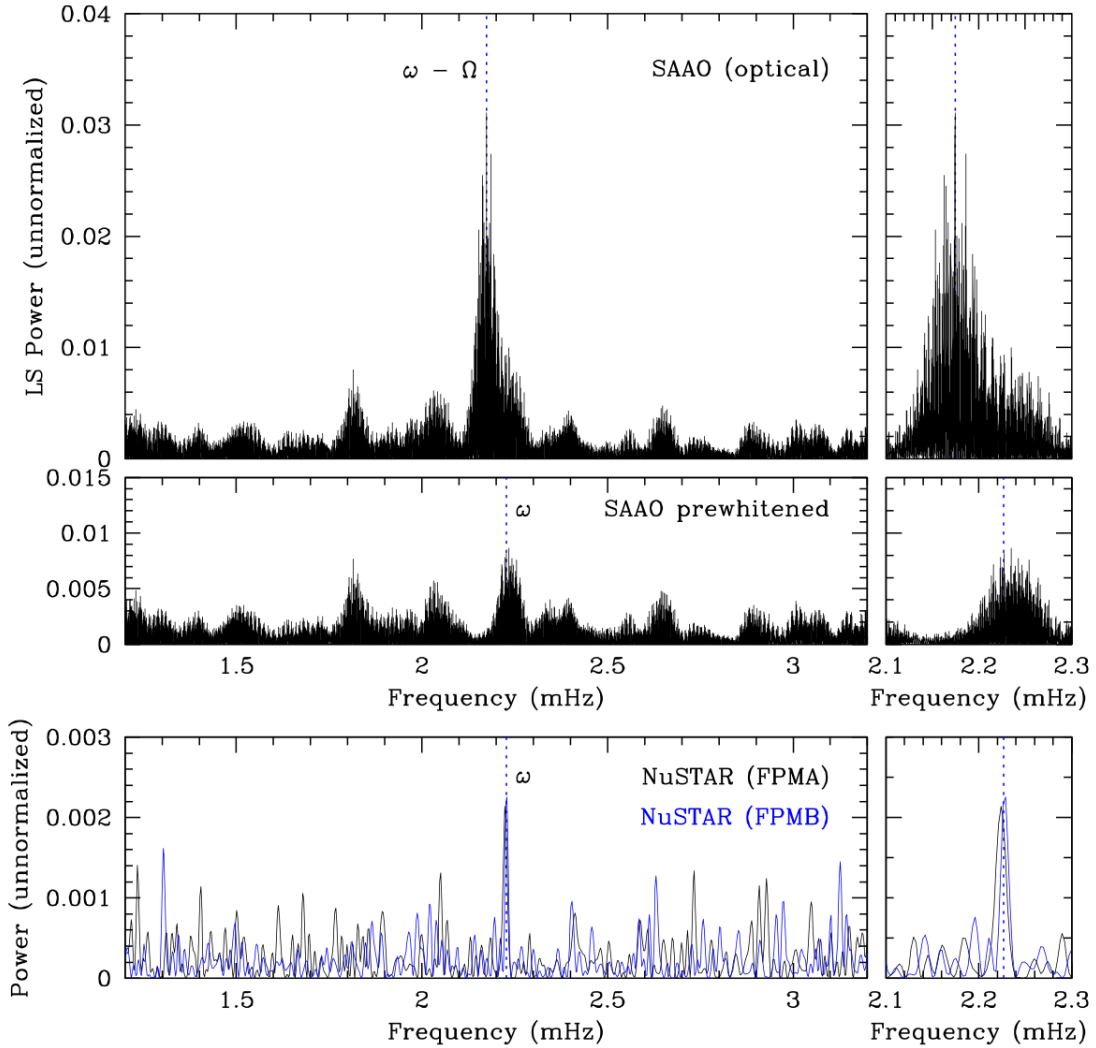


Figure 6. Lomb-Scargle periodograms of the optical data from SAAO (top and middle panels) and the X-ray data from NuSTAR (lower panels). The left panels show the periodogram over a wide frequency range (1.2 - 3.2 mHz), whereas the right panels zoom in on the peaks associated with the spin and the beat frequencies over a narrow frequency range (2.1 - 2.3 mHz). The middle panels show the residual signal after prewhitening with the dominant beat frequency ($\omega - \Omega$) identified in the top panel.

3.4.3. *UV and Optical*

For the *Swift*/UVOT we used the command `uvotsource` in the `heasoft v6.23` to determine the source AB magnitude (uncorrected for extinction); these are reported in column 6 of table 4.

In the *XMM-Newton*/OM, we used the SAS routine `omdetect` (method 1) to find counterparts in the U and UVW1 filters, which were detected at 26.89σ and 8.11σ significance, respectively. These candidate counterparts are $1.10''$ and $1.29''$ from the *Chandra* location, respectively. Both of the sources have nonzero quality and confusion flags, which we address below. The latter is expected in crowded regions like the Galactic plane.

The UVW1-band source is within an area of enhanced emission (possibly diffuse) and has a bad pixel (QFLAG=33). There were also one or more sources detected at a distance of 6–12 pixels (CFLAG=1). Source confusion was checked visually, and the `omdetect` region centroid is centered on the source without significant light from neighboring sources.

The U-band source has the same flags as the UVW1-band, however, it also lies near a bright source (total QFLAG=97) and has one or more sources 3-6 pixels away (total CFLAG=3). The former flag is quite possibly due to the increased sensitivity and spectral breadth compared to the UVW1-band as well as the source lying within

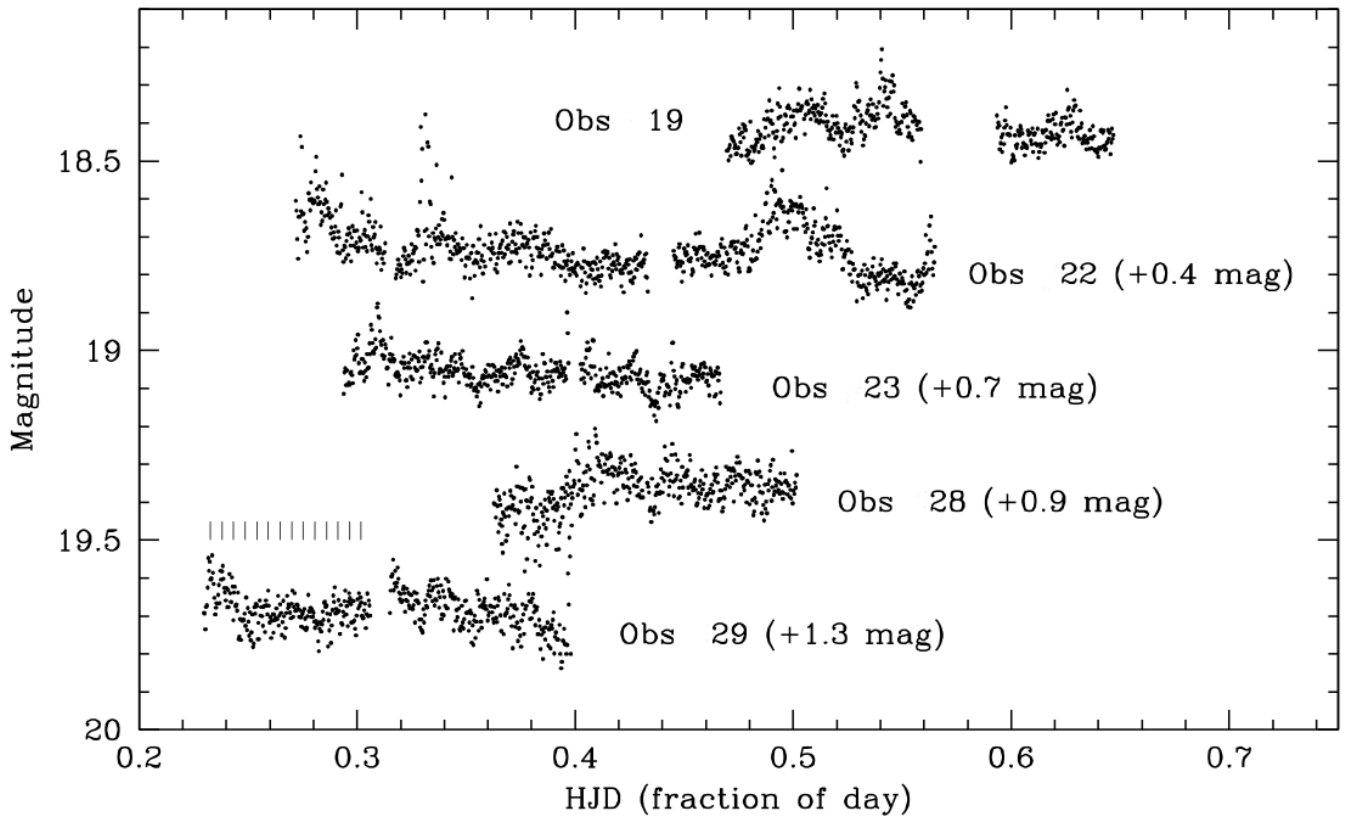


Figure 7. Light curves of J1839 taken with SAAO 1-m telescope. Obs. 19 is shown at the correct brightness, whereas subsequent observing runs have been displaced vertically for display purposes only. The data are calibrated to the Pan-STARRS r-band. The vertical bars for Obs. 29 indicate the expected positions of the spin modulated optical pulses.

Table 4. Observations of Swift J183920.1–045350 by UVOT.

Obs.	ID	Telescope	Start Time [UT] [dd Mmm yyyy hh:mm]	Filter	Magnitude (or 5σ limit) [AB mag]
1.	00044416001	UVOT	21 Mar. 2013 06:59	UVM2	>21.22
2.	00087393001	UVOT	13 Jul. 2017 06:02	UVW1	†
3.	00087393002	UVOT	14 Nov. 2017 02:42	UVW1	†
4.	00010900001	UVOT	01 Oct. 2018 17:09	U	$19.70 \pm 0.15 \pm 0.02$
5.	0821860201	OM	18 Oct. 2018 11:27	UVW1 U	19.67 ± 0.05 18.43 ± 0.02
7.	00088814001	UVOT	02 Nov. 2018 12:30	U	$20.28 \pm 0.10 \pm 0.02$
8.	00088814002	UVOT	08 Nov. 2018 13:34	UVM2	>21.11
10.	00087393003	UVOT	07 Jul. 2019 21:29	UVW1	†

NOTE—*Swift* magnitude uncertainties shown are statistical first (when available) then systematic uncertainty. †: Source projected out of the field of view

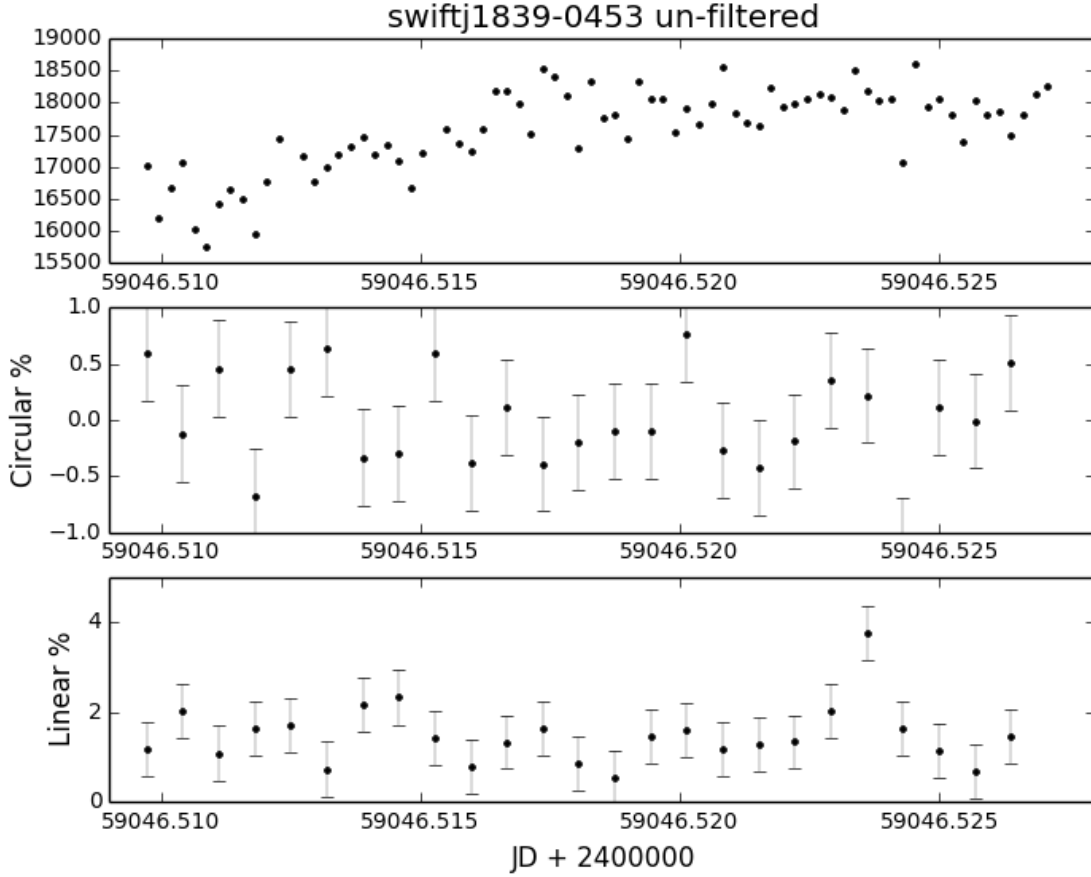


Figure 8. HIPPO photopolarimetry of J1839 taken with SAAO 1.9-m telescope (Obs. 21). The top panel shows total counts and the next two panels show the linear and circular polarization, respectively.

the galactic plane.⁸ Similarly, the source region was visually inspected and deemed acceptable with little neighbor contamination.

3.4.4. Radio

We find no radio sources at or near the *Chandra* position. The closest source, an unidentified radio triple, is $\sim 30''$ away. The 3σ upper limits (i.e., $3 \times \text{rms}$ noise) at the *Chandra* position are 0.043 mJy at 9.746 GHz for Obs. 15; 0.038

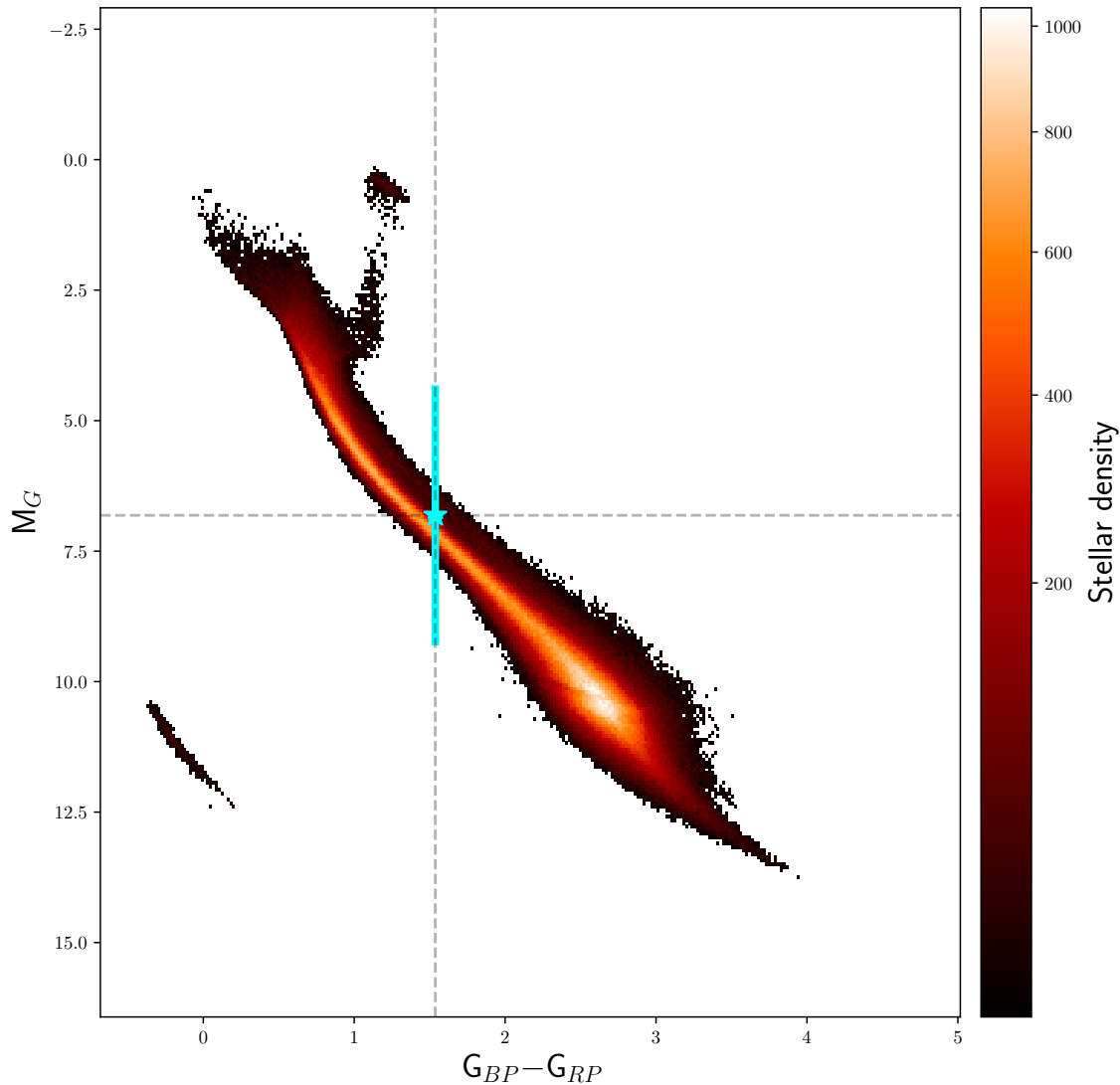


Figure 9. The location of J1839 (cyan) on the Gaia H-R Diagram, using sources ≤ 200 pc from the sun. Other filtering criteria as in Ruiz-Dern et al. (2018).

⁸ See https://xmm-tools.cosmos.esa.int/external/xmm_user_support/documentation/uhb/omfilters.html

Table 5. Fundamental properties of J1839.

Parameter	Value	Citation
Luminosity _{0.4–20 keV}	$2.71^{+2.69}_{-0.91} \times 10^{33}$ erg s ⁻¹	This Work
P_s	449.7 s	This Work
P_o	5.6 ± 0.3 hr	This Work
Distance	$2.3^{+1.9}_{-0.8}$ kpc	Bailer-Jones et al. (2018)
μ_α	-1.1 ± 0.4 mas yr ⁻¹	Gaia Collaboration et al. (2018b)
μ_δ	-2.6 ± 0.4 mas yr ⁻¹	Gaia Collaboration et al. (2018b)

mJy at 9.746 GHz for Obs. 16; and 0.028 mJy at 9.370 GHz for Obs. 17. We combined the data from Obs. 15 – 17 and obtained a 3σ upper limit of 21.6 μ Jy at an effective central frequency of 9.37 GHz with a 2.75 GHz bandwidth.

4. DISCUSSION

The intrinsic properties of J1839 derived above and summarized in Table 5 are typical of known IPs: the X-ray luminosity is typical (Pretorius & Mukai 2014), and the measured spin period and the inferred orbital period are both well within the normal range for IPs (Mukai 2017). Further, the success of our X-ray spectral modeling shows that the X-ray emission may originate in hot plasma, possibly having a multi-temperature nature, that is located next to a cold surface containing Fe of low ionization states. As to the optical magnitude and color, we must first account for interstellar reddening. The 3-d extinction map of Lallement et al. (2019)⁹ only extends to 2.25 kpc in this direction, and gives an extinction of $E_{B-V}=1.08\pm 0.45$ mag at that distance. The lower end of this range may be appropriate for J1839, since the MKCFLOW fits to the X-ray spectrum suggests an interstellar N_H of $3.3^{+1.8}_{-1.6} \times 10^{21}$ cm⁻², or $E_{B-V} \approx 0.5$. Given these uncertainties, it is impossible to be precise, but the location of J1839 in Fig. 9 will shift up and to the left, likely moving it into a location occupied by the majority of IPs as compiled by Abril et al. (2020). Thus, J1839 appears to be a typical IP seen at a larger than typical distance, thus extending the reach of the CV population in our Galaxy.

The discovery of J1839 serves as a reminder that deeper X-ray surveys of the Galactic plane will likely yield detection of an increasing number of IPs. The large majority of currently known IPs have been discovered through X-ray surveys using collimated (non-imaging) instruments, such as Uhuru and HEAO-1, and using coded-mask aperture instruments, Swift BAT and INTEGRAL, perhaps out to distances of 1–2 kpc (Mukai 2017).

The work presented here also demonstrates the feasibility of detecting IPs far away from the Solar neighborhood in a systematic manner. While a number of even more distant IPs have been reported, those close to Galactic center distances are not suitable for detailed multi-wavelength studies such as the one we have performed. Moreover, very distant IPs discovered serendipitously can not be reliably used for statistical population studies. Future DGPS discoveries of IPs have the potential to lead to a direct observational study of the Galactic distribution of CVs, a subject rarely discussed in literature, with a few exceptions, e.g., Britt et al. (2015). Such studies will place the estimates of the CV contributions to the Galactic Ridge on a much firmer ground (Mukai & Shiokawa 1993).

Deep X-ray surveys might also uncover a relatively nearby population of low luminosity IPs (LLIPs), if such objects exist (Pretorius & Mukai 2014). Current indications are that there is a deficit of IPs with X-ray luminosities in the 10^{32} to 10^{33} ergs s⁻¹ range, but perhaps with a separate population of LLIPs below 10^{32} ergs s⁻¹. DGPS and other future X-ray surveys have the potential to confirm or refute this possibility.

5. CONCLUSIONS

We described the multi-wavelength followup of the source J1839, discovered within the scope of the DGPS. We found source counterparts in Gaia and PanSTARRS data which allowed us to determine source location, distance, and proper motion. We detect counterparts to J1839 in the UV, optical, and IR regimes, however no counterpart was found in the radio S or X bands in VLA archival data and our followup observations, respectively.

We found a hard X-ray spectrum with three *Fe* lines. This is fit well with a `mkcflow` spectral model with an additional Gaussian line for neutral *F_e*, which is doubly-absorbed by local and ISM material. We find *H_α* and *He* lines in the optical/IR spectra, the former of which are double-peaked and evolves with time.

⁹ Available online at <https://stilism.obspm.fr/>

In our timing analysis we found two periods, at 449.7 s and 459.89 s which we interpret to be the spin and beat periods of an intermediate polar (IP) magnetic CV system. From these periods we infer an orbital period of 5.6 h. This orbital period is consistent with periods seen with moderate significance in two independent datasets of long-baseline optical photometry (ZTF and SAAO). The orbital, spin and beat period detections provide strong evidence of an intermediate polar (IP) classification for J1839. Other supporting evidence includes the complex nature of the optical emission lines and the presence of He II 4686Å emission. Furthermore, we find a sinusoidal pulse profile in the X-ray data at the spin period, with a pulse fraction that decreases with increasing energy, another characteristic that supports the IP origin of J1839.

Facilities: Swift, NuSTAR, XMM-Newton, Chandra, SALT, SAAO, Gaia, Pan-STARRS, ZTF, APO, VLA

Software: SAS, Pydis, Pyspeckit, Stingray, DS9, Python 3, Heasoft, CASA

REFERENCES

- Abril, J., Schmidtbreick, L., Ederoclite, A., & López-Sanjuan, C. 2020, MNRAS, 492, L40
- An, H., Madsen, K. K., Westergaard, N. J., et al. 2014, in Society of Photo-Optical Instrumentation Engineers (SPIE) Conference Series, Vol. 9144, Space Telescopes and Instrumentation 2014: Ultraviolet to Gamma Ray, 91441Q
- Bailer-Jones, C. A. L., Rybizki, J., Fouesneau, M., Mantelet, G., & Andrae, R. 2018, AJ, 156, 58
- Bayo, A., Rodrigo, C., Barrado Y Navascués, D., et al. 2008, A&A, 492, 277
- Bellm, E. C., Kulkarni, S. R., Graham, M. J., et al. 2019, PASP, 131, 018002
- Buermann, K., Burwitz, V., Reinsch, K., Schwöpe, A., & Thomas, H. C. 2020, arXiv e-prints, arXiv:2010.11678
- Bildsten, L., Chakrabarty, D., Chiu, J., et al. 1997, ApJS, 113, 367
- Britt, C. T., Maccarone, T., Pretorius, M. L., et al. 2015, MNRAS, 448, 3455
- Buccheri, R., Bennett, K., Bignami, G. F., et al. 1983, A&A, 128, 245
- Buckley, D. A. H., Swart, G. P., & Meiring, J. G. 2006, in Proc. SPIE, Vol. 6267, Society of Photo-Optical Instrumentation Engineers (SPIE) Conference Series, 62670Z
- Burgh, E. B., Nordsieck, K. H., Kobulnicky, H. A., et al. 2003, in Proc. SPIE, Vol. 4841, Instrument Design and Performance for Optical/Infrared Ground-based Telescopes, ed. M. Iye & A. F. M. Moorwood, 1463–1471
- Chambers, K. C., Magnier, E. A., Metcalfe, N., et al. 2016, arXiv e-prints, arXiv:1612.05560
- Coppejans, D. 2016, PhD thesis, Radboud University Nijmegen
- Coppejans, D. L., Woudt, P. A., Warner, B., et al. 2014, MNRAS, 437, 510
- Coppejans, R., Gulbis, A. A. S., Kotze, M. M., et al. 2013, PASP, 125, 976
- Crawford, S. M., Still, M., Schellart, P., et al. 2010, in Proc. SPIE, Vol. 7737, Observatory Operations: Strategies, Processes, and Systems III, 773725
- Cropper, M. 1990, SSRv, 54, 195
- de Martino, D., Bernardini, F., Mukai, K., Falanga, M., & Masetti, N. 2020, Advances in Space Research, 66, 1209
- Done, C., & Magdziarz, P. 1998, MNRAS, 298, 737
- Evans, P. A., Osborne, J. P., Beardmore, A. P., et al. 2014, ApJS, 210, 8
- Ezuka, H., & Ishida, M. 1999, ApJS, 120, 277
- Gabriel, C., Denby, M., Fyfe, D. J., et al. 2004, in Astronomical Society of the Pacific Conference Series, Vol. 314, Astronomical Data Analysis Software and Systems (ADASS) XIII, ed. F. Ochsenbein, M. G. Allen, & D. Egret, 759
- Gaia Collaboration, Brown, A. G. A., Vallenari, A., et al. 2018a, A&A, 616, A1
- . 2018b, A&A, 616, A1
- Garmire, G. P., Bautz, M. W., Ford, P. G., Nousek, J. A., & Ricker, George R., J. 2003, in Society of Photo-Optical Instrumentation Engineers (SPIE) Conference Series, Vol. 4851, Proc. SPIE, ed. J. E. Truemper & H. D. Tananbaum, 28–44
- Gorgone, N., & Kouveliotou, C. 2017, in AAS/High Energy Astrophysics Division #16, AAS/High Energy Astrophysics Division, 105.22
- Graham, M. J., Kulkarni, S. R., Bellm, E. C., et al. 2019, PASP, 131, 078001
- Harrison, F. A., Craig, W. W., Christensen, F. E., et al. 2013, ApJ, 770, 103
- Hartman, J. D., & Bakos, G. Á. 2016, Astronomy and Computing, 17, 1
- Hellier, C. 1997, MNRAS, 291, 71
- Hellier, C., & Mukai, K. 2004, MNRAS, 352, 1037

- Hellier, C., Mukai, K., & Osborne, J. P. 1998, *MNRAS*, 297, 526
- Huppenkothen, D., Bachetti, M., Stevens, A. L., et al. 2019, *ApJ*, 881, 39
- Jansen, F., Lumb, D., Altieri, B., et al. 2001, *A&A*, 365, L1
- Lallement, R., Babusiaux, C., Vergely, J. L., et al. 2019, *A&A*, 625, A135
- Littlefield, C., Garnavich, P., Kennedy, M. R., et al. 2016, *ApJ*, 833, 93
- Lopes de Oliveira, R., & Mukai, K. 2019, *ApJ*, 880, 128
- Madsen, K. K., Grefenstette, B. W., Pike, S., et al. 2020, *arXiv e-prints*, arXiv:2005.00569
- Masci, F. J., Laher, R. R., Rusholme, B., et al. 2019, *PASP*, 131, 018003
- Mason, K. O., Breeveld, A., Much, R., et al. 2001, *A&A*, 365, L36
- McClintock, J. E., Canizares, C. R., & Tarter, C. B. 1975, *ApJ*, 198, 641
- Mukai, K. 2017, *PASP*, 129, 062001
- Mukai, K., & Shiokawa, K. 1993, *ApJ*, 418, 863
- Pala, A. F., Gänsicke, B. T., Breedt, E., et al. 2020, *MNRAS*, 494, 3799
- Patterson, J. 1994, *PASP*, 106, 209
- Potter, S. B., Buckley, D. A. H., O'Donoghue, D., et al. 2010, *MNRAS*, 402, 1161
- Pretorius, M. L. 2009, *MNRAS*, 395, 386
- Pretorius, M. L., & Mukai, K. 2014, *MNRAS*, 442, 2580
- Roming, P. W. A., Kennedy, T. E., Mason, K. O., et al. 2005, *SSRv*, 120, 95
- Ruiz-Dern, L., Babusiaux, C., Arenou, F., Turon, C., & Lallement, R. 2018, *A&A*, 609, A116
- Strüder, L., Briel, U., Dennerl, K., et al. 2001, *A&A*, 365, L18
- Turner, M. J. L., Abbey, A., Arnaud, M., et al. 2001, *A&A*, 365, L27
- Warner, B. 1986, *MNRAS*, 219, 347
- Warner, B. 1992, in *Astronomical Society of the Pacific Conference Series*, Vol. 29, *Cataclysmic Variable Stars*, ed. N. Vogt, 242
- Warner, B. 1995, *Cataclysmic Variable Stars*, Cambridge Astrophysics (Cambridge University Press), doi:10.1017/CBO9780511586491
- Wickramasinghe, D. 2014, in *European Physical Journal Web of Conferences*, Vol. 64, *European Physical Journal Web of Conferences*, 03001

Acknowledgements: The authors wish to thank Sylvia Rose Kowalski and Deena Mickelson for their roles in VLA data acquisition. They also thank Hannes Breytenbach for taking some of the SAAO data. PAW acknowledges financial support from the University of Cape Town and the National Research Foundation. The SALT observations reported here were obtained through the SALT Large Science program 2018-2-LSP-001, with D.B. as PI, who also acknowledges support of the National Research Foundation. C.K., and N.G. acknowledge support under NASA Grant 80NSSC19K0916 and Smithsonian Astrophysical Observatory Grant GO9-20057X. B.O. is supported in part by the National Aeronautics and Space Administration through grants NNX16AB66G, NNX17AB18G, and 80NSSC20K0389.

We thank the NRAO for the generous allocation of VLA time for our observations. The National Radio Astronomy Observatory is a facility of the National Science Foundation operated under cooperative agreement by Associated Universities, Inc.

This work has made use of data from the European Space Agency mission Gaia (<https://www.cosmos.esa.int/gaia>), processed by the Gaia Data Processing and Analysis Consortium (DPAC, <https://www.cosmos.esa.int/web/gaia/dpac/consortium>). Funding for the DPAC has been provided by national institutions, in particular the institutions participating in the Gaia Multilateral Agreement.